PCCP

ROYAL SOCIETY OF CHEMISTRY

PAPER





Cite this: *Phys. Chem. Chem. Phys.*, 2024, **26**, 8408

# Cyclic ion mobility of doped $[MAu_{24}L_{18}]^{2-}$ superatoms and their fragments (M = Ni, Pd and Pt; L = alkynyl)†

Frank Hennrich,[ad] Shun Ito,[b] Patrick Weis,[a] Marco Neumaier,[ac] Shinjiro Takano,[b] Tatsuya Tsukuda[b] and Manfred M. Kappes*[acd]

Received 20th December 2023,
Accepted 19th February 2024

DOI: 10.1039/d3cp06192b

rsc.li/pccp

Collision-induced dissociation and high-resolution cyclic ion mobility mass spectrometry, along with quantum chemical calculations and trajectory simulations, were used to compare the structures of isolated $[MAu_{24}(C{\equiv}CR)_{18}]^{2-}$, M = Ni, Pd, or Pt, and their associated fragment ions. The three different alkynyl ligand-stabilized (C≡CR, R = 3,5-$(CF_3)_2C_6H_3$), transition metal-doped, gold cluster dianions showed mutually resolvable collision cross sections (CCS), which were ordered consistently with their molecular structures from X-ray crystallography. All three $[MAu_{24}(C{\equiv}CR)_{18}]^{2-}$ species fragment by sequential diyne loss to form $[MAu_{24}(C{\equiv}CR)_{18-n}]^{2-}$, with $n$ up to 12. The resultant fragment isomer distributions are significantly $n$- and M-dependent, and hint at a process involving concerted elimination of adjacent ligands. In particular $[NiAu_{24}(C{\equiv}CR)_{18}]^{2-}$ also fragments to generate alkyne-oligomers, an inference supported by the parallel observation of precursor dianion isomerization as collision energy is increased.



## 1. Introduction

Doped elemental clusters often form cage-like structures enclosing atomic or molecular dopants. Endohedrally doped fullerene carbon cages were among the first examples. Analogous centrally doped clusters are known for many other elements.[1–4] For example, naked (*i.e.* ligand-free) gold clusters caging different transition metal atoms have been extensively studied in rarified molecular beam experiments and by quantum chemical calculations.[5] It has also become possible to stabilize such transition metal doped gold clusters using a shell of organic ligands.[6–9] In contrast to bare gold clusters, the "coating" with a finite number of ligands provides sufficient protection of the cluster cores to prevent them from coalescing. Consequently air-stable, ligand-stabilized, gold clusters centrally doped with transition metal atoms can be made in bulk quantities and studied at a level of detail going much beyond molecular beam experiments.

The recently established "$MAu_{24}L_{18}$ series" (M = Ni, Pd and Pt) is a prototypical example of single-atom doped gold clusters stabilized by ligands L, such as thiolates (SR) and alkynyls (C≡CR).[10–17] The geometric structure of $MAu_{24}L_{18}$ clusters including the location of dopant M was determined by X-ray crystallography. The three $[MAu_{24}(C{\equiv}CR)_{18}]^{2-}$ dianions (M = Ni, Pd, Pt; R = 3,5-$(CF_3)_2C_6H_3$) share a common molecular structure as exemplified in Scheme 1 for M = Ni. The central heteroatom M (green) is surrounded by an icosahedral shell of 12 gold atoms (yellow). This icosahedron is protected by six staples each comprising discrete $Au_2(C{\equiv}CR)_3$ units (bronze Au atoms) which can be thought of as holding the core together against isomerization. There are small systematic changes in M–Au bond lengths as the dopant is varied – reflecting to first order the different sizes of the central heterometal atoms.

The different $[MAu_{24}(C{\equiv}CR)_{18}]^{2-}$ species, which from here on we will generally refer to as $MAu_{24}$, also share a common electronic structure as inferred from DFT (density functional theory) calculations of the isolated dianions and from various experimental results. According to an interpretation based on the spherical jellium model of simple metal clusters,[18–20] the isolated ground state species correspond to 8-electron superatoms with eight $s^1$-electrons delocalized over the icosahedral core (counting rule: 24 (Au) + 0 (M) − 18 (L) + 2 (dianion) = 8, *i.e.* $1S^2$ + $1P^6$). Interestingly, in this counting of delocalized

[a] *Institute of Physical Chemistry, Karlsruhe Institute of Technology, Fritz-Haber-Weg 2, Karlsruhe 76131, Germany. E-mail: manfred.kappes@kit.edu*
[b] *Department of Chemistry, Graduate School of Science, The University of Tokyo, 7-3-1 Hongo, Bunkyo-ku, Tokyo 113-0033, Japan*
[c] *Institute of Nanotechnology, Karlsruhe Institute of Technology, Hermann-von-Helmholtz-Platz 1, Eggenstein-Leopoldshafen 76344, Germany*
[d] *Institute of Quantum Materials and Technologies, Karlsruhe Institute of Technology, Hermann-von-Helmholtz-Platz 1, Eggenstein-Leopoldshafen 76344, Germany*

† Electronic supplementary information (ESI) available. See DOI: https://doi.org/10.1039/d3cp06192b

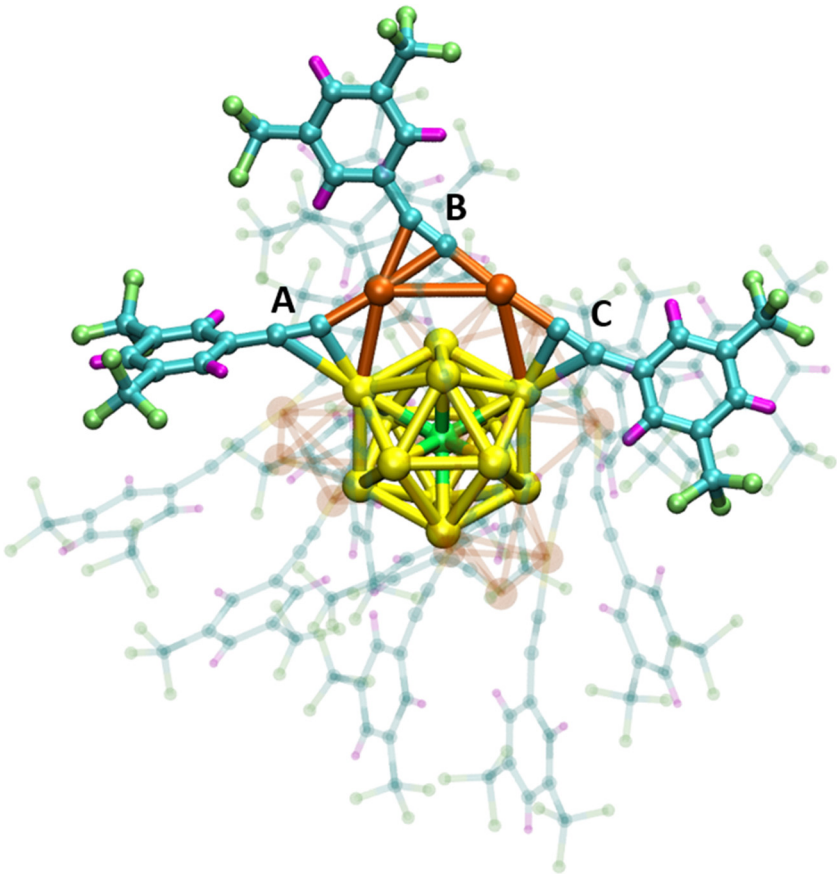


Scheme 1 $[NiAu_{24}(C{\equiv}CR)_{18}]^{2-}$ structure as determined by X-ray crystallography (R = 3,5-$(CF_3)_2C_6H_3$ (3,5-bis(trifluoromethyl)phenyl)).[12] The icosahedral $NiAu_{12}$ cluster core with central heteroatom is surrounded by six $Au_2(C{\equiv}CR)_3$ staples one of which is highlighted. Each staple comprises three ($C{\equiv}CR$) ligands labelled A, B and C. Color coding: Au (yellow (icosahedral shell) and bronze (staples)), C (blue), H (pink), F (lime green) and Ni (green). $[PdAu_{24}(C{\equiv}CR)_{18}]^{2-}$ and $[PtAu_{24}(C{\equiv}CR)_{18}]^{2-}$ have the same molecular structure with slightly different bond lengths.

electrons, the group 10 metal atom at the center does not contribute to the number of delocalized valence electrons. In a cross section through the center of the positive jellium background this can be rationalized by raising the potential of the central region relative to the perimeter (two-step jellium model).[21–24] This destabilizes the 1S shell relative to 1P and 1D shells, but not enough to change the $1S^2 + 1P^6$ filling order.

The establishment of a synthesis route to ligand stabilized $MAu_{24}$ clusters has been significantly aided by electrospray ionization (ESI) mass spectrometry. $[MAu_{24}(C{\equiv}CR)_{18}]^{2-}$ dianions are the primary gold-containing species observed in the ESI mass spectra of a solution of $[MAu_{24}(C{\equiv}CR)_{18}](PPh_4)_2$. It is interesting to consider whether these isolated dianions have the same molecular structures as the $MAu_{24}$ clusters making up the single crystals. Perhaps there are structure changes upon solvation and electrospraying? Clusters in the crystalline solid may undergo structural relaxation due to interactions with solvent molecules, counterions and also other proximal clusters – which are missing under isolated conditions. On the other hand, highly charged ions can unravel dynamically in gas phase relative to their solution forms (in which localized excess charges are better shielded from each other by the surrounding dielectric medium).[25]

Here we use ultrahigh resolution cyclic ion mobility spectrometry combined with mass spectrometry (cIMS-MS) to compare the solid-state structures with the gas phase collision cross sections (CCS) of precursor $MAu_{24}$ dianions, M = Ni, Pd and Pt – the so far most highly resolved CCS measurements of ligand stabilized coinage metal clusters. In combination with DFT modelling and trajectory method simulations of the experimental CCS values we find that the ''size'' of the isolated dianions closely follows the M–Au bond length trend observed by X-ray crystallography in solid state.

Isolation of molecular ions in gas phase also offers the possibility to controllably excite them by collisions with an inert gas without accessing dissipative processes involving neighboring molecules (*e.g.* cluster–cluster reactions) as would occur upon thermal treatment in condensed phase environments. In this study, we have used this capability also to compare the structural stability of $MAu_{24}$ towards isomerization and fragmentation as internal excitation levels are incrementally raised. Specifically, we have performed energy dependent CID (collision induced dissociation) measurements and have determined CCS values for precursor dianions and the resulting fragments using cIMS-MS. While, sequential diyne ($RC{\equiv}C{-}C{\equiv}CR$) loss is the dominant common

fragmentation channel for all M, we find $E_{50}$ values (50% survival yield) and fragment CCS values to be M dependent. For M = Ni, collisional excitation also accesses significant ligand oligomer loss.

Below we describe our results and provide first order structural rationalizations based on DFT and semiempirical calculations (of the electronic ground states) as well as ion trajectory simulations of the corresponding orientationally averaged collision cross sections.

## 2. Methods

### 2.1 Synthesis

Cluster samples were synthesized at U. Tokyo as described in detail in SI. $[PdAu_{24}(C{\equiv}CR)_{18}]^{2-}$ and $[PtAu_{24}(C{\equiv}CR)_{18}]^{2-}$ were synthesized by hydride-mediated transformation of presynthesized $[PdAu_8(PPh_3)_8]^{2+}$ and $[PtAu_8(PPh_3)_8]^{2+}$,[11,26–28] respectively. In brief, $[PdAu_{24}(C{\equiv}CR)_{18}]^{2-}$ was obtained by the reaction of Au–C$\equiv$CR polymer complexes and $[PdHAu_8(PPh_3)_8]^{+}$ generated by the reaction between $[PdAu_8(PPh_3)_8]^{2+}$ and $NaBH_4$.[11] The synthetic procedure for $[PtAu_{24}(C{\equiv}CR)_{18}]^{2-}$ was the same except for the use of $[PtAu_8(PPh_3)_8]^{2+}$ instead of $[PdAu_8(PPh_3)_8]^{2+}$. $[NiAu_{24}(C{\equiv}CR)_{18}]^{2-}$ was synthesized by the reaction of Au–C$\equiv$CR polymer complexes and crude $[NiHAu_8(PPh_3)_8]^{+}$.[12] The samples of $[MAu_{24}(C{\equiv}CR)_{18}]^{2-}$ (M = Ni, Pd and Pt) were obtained as $PPh_4^{+}$ salts in a pure form by reprecipitation procedure. The samples were characterized by mass spectrometry and UV-vis spectroscopy.

### 2.2 ESI-MS and cyclic IMS-MS.

Materials were dissolved in MeOH/acetonitrile (1 : 2) at typical concentrations of 0.1 mg $mL^{-1}$ and electrosprayed into a Waters Select Series Cyclic IMS ion mobility mass spectrometer at KIT for further study. Gold containing charged species were only observed in the negative ion mode. By far the most dominant anions observed by high resolution mass spectrometry under standard analytical electrospray conditions were $[MAu_{24}(C{\equiv}CR)_{18}]^{2-}$, M = Ni, Pd and Pt. In the following, we focus on these precursor ions and their anionic fragments as generated by collisional activation.

The Waters Select Series Cyclic IMS ion mobility mass spectrometer can be run in several different standard modes. The setup and working principle of this apparatus which allows for CID, ultrahigh resolution cyclic ion mobility spectrometry cIMS and iterative CID-IMS ($cIMS^n$) measurements each combined with high resolution mass spectrometry have been extensively described.[29] Further details in particular of components and procedures relevant for this study are given in ESI.† Here we used the instrument for: (i) solution analytics by measuring high resolution ESI mass spectra under soft ionization conditions (achievable mass resolution, $m/\Delta m$ of $>100\,000$) while bypassing the cyclic ion mobility separation device (cIM), (ii) collisional activation and fragment mass analysis as a function of collision energy (also bypassing the cIM), (iii) cIMS of mass-range selected precursor dianions to yield arrival time distributions (ATD's) upon one or more cIM cycles and (iv) collisional activation coupled with cIMS and $m/z$ measurements as described. The collisional activation is performed in the ion trap located behind the quadrupole mass filter, the collision gas is nitrogen at a pressure of $2.6 \times 10^{-2}$ mbar, *i.e.* multiple collision conditions.

Cyclic-IMS is one of several commercially available instrumental variants coupling ion mobility spectrometry with high resolution mass spectrometry. In its simplest form IMS measures the drift time of an ion pulled by a static electric field through a finite length drift cell filled with an inert collision gas. This drift time is inversely proportional to the ions' mobility which can be converted to a collision cross section using the Mason–Schamp equation[30] (see ESI†). Such (orientationally averaged) CCS values provide first order structural information for the molecular ion of interest. State-of-the-art IMS instrumental platforms seek to achieve high sensitivities combined with highest mass and ion mobility resolutions. Some of us have previously used and extensively described trapped ion mobility spectrometry (tims) which offers CCS resolutions (CCS/ΔCCS) of up to *ca.* 200 as implemented in a Bruker timsTOFMS. In the present study we make use of a Waters Cyclic IMS which is a comparatively new addition to the arsenal of commercialized IMS methods and can provide significantly higher CCS resolution. cIMS uses travelling wave (TWIMS) excitation to push the ions to be analysed through a cyclic drift cell filled with molecular nitrogen. This allows to extend separation lengths relative to a linear TWIMS cell simply by cycling the ions multiple times. Concretely, in the Waters Cyclic IMS system ions are pulsed into the *ca.* 1 m length cIM device, undergo a selected number of cycles which can range up to more than 50 and are then pulse extracted from the drift tube for mass analysis to yield ATD's as a function of mass-to-charge ratio. The ATD's are then converted to calibrated collision cross sections using a procedure described in detail in ESI.† According to the IMS nomenclature convention they are denoted as $^{tw}CCS_{N2}$ values. According to ref. 29 cIMS can achieve $^{tw}CCS_{N2}$ resolutions of more than 750 as ultimately limited by self-diffusion and collisional broadening of the ion packets injected into the cIM. We will separately report on $^{tw}CCS_{N2}$ calibration and dependence of resolution on TWIMS parameters in a future publication – including a comparison to $^{tims}CCS_{N2}$ values for a variety of substance classes and molecular ion charge states.[31]

For measurements of the high $m/z$ monoanionic fragments generated upon CID of $[NiAu_{24}(C{\equiv}CR)_{18}]^{2-}$ we used a Bruker compact ESI-MS optimized for high $m/z$ detection (at U. Tokyo).

### 2.3 Theory

Experimental $^{tw}CCS_{N2}$ values were compared to predictions, $^{theo}CCS_{N2}$, from trajectory method simulations using the IMoS 1.09 package[32,33] (see ESI† for further details). These simulations were based on model structures obtained from DFT calculations performed with TURBOMOLE 7.4[34] using the PBE functional[35–38] with def2-SVP basis sets[39] and accounting for dispersion interactions at the DFT-D3 bj level.[40,41] To prevent SCF (self-consistent-field) convergence problems we used Fermi

 

smearing as implemented in TURBOMOLE. For calculating partial charges of some model structures we also used semi-empirical extended tight binding calculations, *i.e.* the GFN 1 *x*TB-method.[42,43] For the three $[MAu_{24}(C{\equiv}CR)_{18}]^{2-}$ precursor dianions, starting structures were taken as corresponding to the published X-ray crystal based DFT structure 0a[44] of $[PdAu_{24}(C{\equiv}CR)_{18}]^{2-}$ (*i.e.* with central heteroatom surrounded by 12 gold atoms oriented in an icosahedral shell) and further geometry optimized with DFT without symmetry constraints. For $[PtAu_{24}(C{\equiv}CR)_{18}]^{2-}$ and $[NiAu_{24}(C{\equiv}CR)_{18}]^{2-}$ we swapped the central metal atom. The resulting relaxed structures share basically the same geometry as the X-ray structures, except for a small overall contraction (3–4% for $[NiAu_{24}(C{\equiv}CR)_{18}]^{2-}$, $[PdAu_{24}(C{\equiv}CR)_{18}]^{2-}$ and $[PtAu_{24}(C{\equiv}CR)_{18}]^{2-}$). The contraction mainly occurs in the ligand shell reflecting minor changes in the ligand orientations and slightly shorter Au–C bonds upon geometry optimization. The root mean square deviation between the $[MAu_{24}(C{\equiv}CR)_{18}]^{2-}$ X-ray structures[11,12] and our DFT optimized structures of isolated $[MAu_{24}(C{\equiv}CR)_{18}]^{2-}$ is 0.92 Å (M = Ni), 0.81 Å (M = Pd) and 0.86 Å (M = Pt), respectively, as determined with Jmol[45] and RMSD.[46] Comparing only the $MAu_{24}$ metal cores a deviation of 0.19 Å is determined for $PdAu_{24}$ and $PtAu_{24}$ and 0.20 Å for $NiAu_{24}$, showing that most of the changes occur in the ligand shell and not in the metal core. To compare to experiment, relaxed DFT structures were translated into the corresponding $^{theo}CCS_{N2}$ values *via* trajectory calculations (see ESI†).

Selected fragments $[MAu_{24}(C{\equiv}CR)_{18-n}]^{2-}$ were investigated by iteratively removing ligands from the corresponding $[MAu_{24}(C{\equiv}CR)_{18}]^{2-}$ DFT structure in a variety of different ways designed to simulate either statistical or non-statistical fragmentation behavior as described in detail below (and in ESI†). The $^{theo}CCS_{N2}$ of the resulting unrelaxed structures were then calculated with IMoS by using partial charges obtained from GFN 1 *x*TB calculations (see ESI†). Structures were visualized with VMD[47] and Jmol.[45]

# 3. Results and discussion

### 3.1 Separating $[MAu_{24}(C{\equiv}CR)_{18}]^{2-}$ precursor ions according to their ion mobility

Assuming that the known crystal structures are essentially retained in gas phase we expected the three $MAu_{24}$ precursor dianions to have very close lying $^{tw}CCS_{N2}$, close to the instrumental resolution of our cIM. To minimize small perturbations due to temperature and pressure fluctuations in the cIM, we therefore explored their relative size using a mixture – *i.e.* essentially with an internal reference. For this all three dianions were softly injected into the cIM device together and then separated from each other in up to 50 cycles, pulse extracted from the cIM and subsequently mass analyzed (much as in a recirculating HPLC analysis with specific optical detection).[48]

Fig. 1 shows a partial mass spectrum of the mixture used – containing $[MAu_{24}(C{\equiv}CR)_{18}]^{2-}$ with M = Ni, Pd and Pt in the relative ratios 2.7 : 1.3 : 1. Fig. 2 shows arrival time distributions

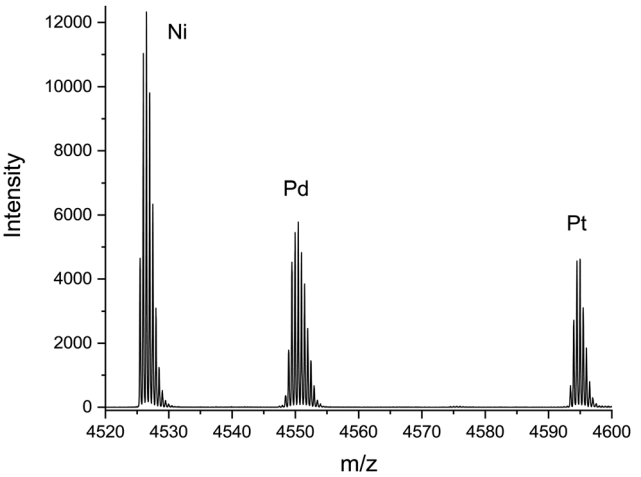


Fig. 1 Electrospray ionization mass spectrum obtained for the mixture of $[MAu_{24}(C{\equiv}CR)_{18}]^{2-}$, M = Ni, Pd and Pt, which was used to obtain their orientally averaged collision cross sections in molecular nitrogen, $^{tw}CCS_{N2}$, as shown in Fig. 2 and Table 1. See ESI† for comparison of resolved experimental isotope distributions to simulations for natural isotope abundances.

obtained for this mixture at different numbers of separation cycles ranging from 1–50 as indicated (left – integrating over the full mass range from $m/z$ = 4520–4600, *i.e.* encompassing all three precursor dianions; and right mass- and therefore M-selective arrival times for the case of a 50 cycle separation). With increasing numbers of cycles in Fig. 2 (left), three peaks begin to separate corresponding to the three different $[MAu_{24}(C{\equiv}CR)_{18}]^{2-}$ species contained in the mixture (as confirmed by relative ion intensities and concurrent $m/z$ analysis). Note that 50 cycles correspond to an overall drift length of 50 m. The dianions arrive at the extraction point (equivalent to a column elution in chromatography) in the sequence Ni < Pd < Pt. Thus, the size trend seen in solid state is also retained in gas phase.

Note, that the 50 cycle separation shown in Fig. 2 corresponds to a CCS resolution of about 300. Even higher CCS resolutions could be obtained by cycling further. Achievable resolution is however ultimately limited by the finite cIM ring circumference of ~1 m: eventually the lower CCS (and thus faster) ions begin to catch up to the higher CCS (and thus slower) ions. Note also, that under our conditions $MAu_{24}$ ion intensity decays roughly by 3.7% per pass of the cIM device.

Based on multiple such 50 cycle measurements (on $MAu_{24}$ mixtures probed under similar conditions on different days and calibrated against 50 cycle separations of Agilent Tunemix monoanions some of which also lie in the same $m/z$ range) we determined absolute $^{tw}CCS_{N2}$ values of 721.5, 723.3 and 724.9 Å$^2$ for $NiAu_{24}$, $PdAu_{24}$ and $PtAu_{24}$ with an error of ± 0.8 Å$^2$ whereas the difference between peaks can be measured with higher precision and is 1.80 ± 0.1 Å$^2$ between $NiAu_{24}$ and $PdAu_{24}$ and 1.63 ± 0.1 Å$^2$ between $PdAu_{24}$ and $PtAu_{24}$. To analyze the data, Gaussian functions were fitted to the mass-resolved ATD's. The corresponding maxima were then converted to calibrated $^{tw}CCS_{N2}$ values. Error bars reflect statistical

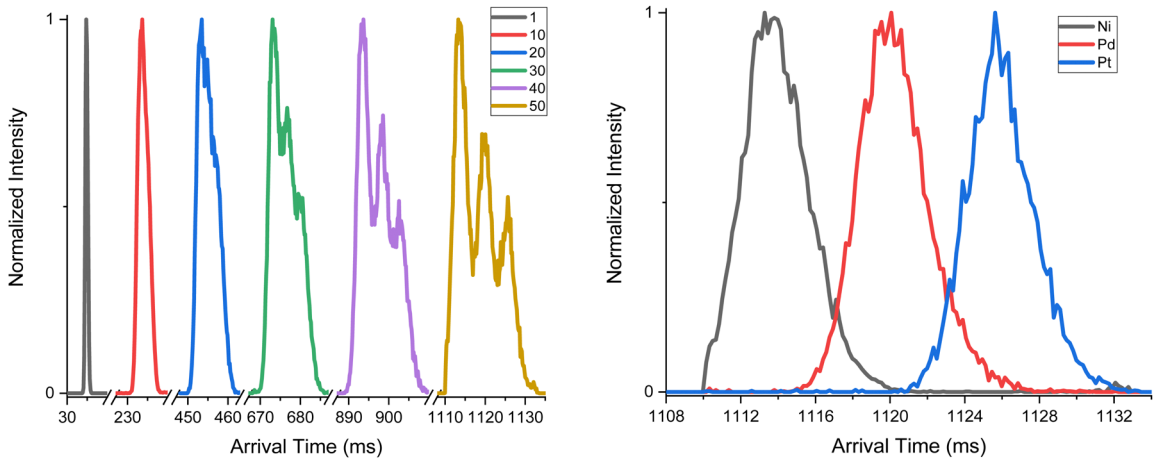


Fig. 2 Cyclic-IMS separations obtained for a mixture of $[MAu_{24}(C{\equiv}CR)_{18}]^{2-}$, M = Ni, Pd and Pt (see Fig. 1). Left: Arrival time distributions (ATD's) for all $[MAu_{24}(C{\equiv}CR)_{18}]^{2-}$ ions together obtained by integrating over the $m/z$ = 4520–4600 range – as a function of the number of separation cycles from 1–50. Right – M-specific arrival time distributions for 50 separation cycles, *i.e.* recorded for the $m/z$ range corresponding to the isotopologues of a specific $[MAu_{24}(C{\equiv}CR)_{18}]^{2-}$ and normalized to the respective ATD maxima. The ATD's can be converted to orientationally averaged collision cross sections, $^{tw}CCS_{N2}$ of the three different gas phase dianions, see text. Note that the order of elution, Ni < Pd < Pt, is consistent with the size trend in condensed phase.

Table 1 Comparison of $^{tw}CCS_{N2}$ for isolated $[MAu_{24}(C{\equiv}CR)_{18}]^{2-}$ with calculated $^{theo}CCS_{N2}$ values (see text and Fig. S1, ESI)

| | $^{tw}CCS_{N2}$/Å$^2$ | $^{theo}CCS_{N2}$/Å$^2$ DFT structure/DFT charges | $^{theo}CCS_{N2}$/Å$^2$ DFT structure/GFN1 *x*TB charges | Deviation[a]/% |
|---|---|---|---|---|
| $[PtAu_{24}(C{\equiv}CR)_{18}]^{2-}$ | 724.9 ± 0.8 | 730.5 ± 0.4 | 724.0 ± 0.3 | 0.7, −0.13 |
| $[PdAu_{24}(C{\equiv}CR)_{18}]^{2-}$ | 723.3 ± 0.8 | 730.4 ± 0.3 | 723.4 ± 0.4 | 1.0, 0.02 |
| $[NiAu_{24}(C{\equiv}CR)_{18}]^{2-}$ | 721.5 ± 0.8 | 728.3 ± 0.4 | 721.0 ± 0.3 | 0.9, −0.07 |

[a] Deviation between column 1 and 2 and column 1 and 3, respectively.

fluctuations in the positions of the maxima of the Gaussians from one cIM injection to the next.

Table 1 compares experimental and theoretical CCS values (calculated starting from the X-ray based DFT structure of $[PdAu_{24}(C{\equiv}CR)_{18}]^{2-}$ – see above) for the gas phase precursor dianions. With $^{theo}CCS_{N2}$ values of 730.5 Å$^2$ (M = Pt), 730.4 Å$^2$ (M = Pd) and 728.3 Å$^2$ (M = Ni), the experimental $^{tw}CCS_{N2}$ values are reproduced to within 1%. The standard error (*i.e.* the statistical uncertainty) of $^{theo}CCS$ was determined to ±0.3 Å$^2$ from at least 10 different trajectory simulation runs (each with *ca.* 3 million trajectories with varying starting orientation, see ESI†). Additionally, in order to address sources of systematic error, we list $^{theo}CCS_{N2}$ of the DFT structures but using Mulliken partial charges from GFN1 *x*TB as we used this method for calculating $^{theo}CCS$ of the fragment isomers (see below). When using Mulliken charges from *x*TB, the $^{theo}CCS$ values agree even better with the experimental data (presumably due to error compensation as Mulliken results in unphysically negative partial charges for the central metal atom). The decreasing $^{theo}CCS_{N2}$ from Pt to Ni is well correlated with (the DFT computed) decreasing distances from the central atom M to the icosahedral Au atoms of 2.81 Å (Pt–$Au_{ico}$) and 2.76 Å (Ni–$Au_{ico}$). The $^{theo}CCS_{N2}$ of the Pt and Pd containing cluster are very similar as are the distances of 2.81 Å (Pt–$Au_{ico}$) and 2.80 Å (Pd–$Au_{ico}$). In general, agreement of theory and experiment to within 1% is surprisingly good for molecules of this size and complexity. In previous tims studies of related molecules in this size range we have typically achieved agreement to within 2%.[49,50] This is a strong indicator, that in the $MAu_{24}$ dianions, transfer into gas phase does not significantly change the bond connectivity or relative bond orientations.

### 3.2 Collision induced dissociation

The authors of ref. 10 inferred from their CID MS measurements and DFT calculations, that collisionally excited $[PtAu_{24}(C{\equiv}CR)_{18}]^{2-}$ and $[PdAu_{24}(C{\equiv}CR)_{18}]^{2-}$ (R = 3,5-$(CF_3)_2C_6H_3$) can sequentially eliminate neutral 1,3-diynes (RC≡C–C≡CR), *i.e.* concerted loss of two C≡CR units at a time, to generate $[MAu_{24}(C{\equiv}CR)_{18-n}]^{2-}$, with even $n$ = 2–12, reaction (1).

$$[MAu_{24}(C{\equiv}CR)_{18}]^{2-*} \rightarrow [MAu_{24}(C{\equiv}CR)_{16}]^{2-} + RC{\equiv}C{-}C{\equiv}CR \rightarrow [MAu_{24}(C{\equiv}CR)_{14}]^{2-} + RC{\equiv}C{-}C{\equiv}CR \rightarrow \ldots \quad (1)$$

In a minor additional fragmentation channel, *one* HC≡CR molecule may sometimes also be lost – to generate $[MAu_{24}(C{\equiv}CR')(C{\equiv}CR)_{17-n}]^{2-}$, (R′ = 3,5-$(CF_3)_2C_6H_2$) with overall odd numbered $n$ = 1–11. Remarkably, dianions were found to be the dominant fragment charge state (only

 

comparatively small amounts of monoanions were additionally detected) and these always retained an intact $MAu_{24}$ metal cluster moiety – *i.e.* the cleaved/reacted ligands did not significantly carry away any excess charge or metal atoms.

In the present study, we have confirmed the $[PtAu_{24}(C{\equiv}CR)_{18}]^{2-}$ and $[PdAu_{24}(C{\equiv}CR)_{18}]^{2-}$ measurements of ref. 10 and have now also probed the corresponding CID phenomenology of $[NiAu_{24}(C{\equiv}CR)_{18}]^{2-}$ (see Fig. S3 and S4, ESI†). At intermediate to high collision energies, we find fragments analogous to those observed for M = Pt and Pd, *i.e.* $[NiAu_{24}(C{\equiv}CR)_{18-n}]^{2-}$ and $[MAu_{24}(C{\equiv}CR')(C{\equiv}CR)_{17-n}]^{2-}$. There is however one interesting difference. Significant ligand oligomer monoanion formation is also seen (for odd $n$ = 5–9: $(C{\equiv}CR)_n^-$; for even $n$ = 4–10: $(C{\equiv}CR)_n^-$ plus some $[(C{\equiv}CR)_n \pm H]^-$) – already at low collision energies. While trace amounts of $(C{\equiv}CR)_n^-$ can also be seen upon collisional excitation of $PtAu_{24}$ and $PdAu_{24}$ (upon closer inspection), for $NiAu_{24}$ the polymer intensity is at least two orders of magnitude larger and extends to a remarkably high $n > 10$. Note, that CID measurements on a Bruker compact ESI-MS platform optimized for the detection of high $m/z$ species indicate that the complementary monoanionic molecular fragments comprise $[NiAu_{24}(C{\equiv}CR)_{18-n}]^-$, reaction (2) (see Fig. S5, ESI†).

$$[MAu_{24}(C{\equiv}CR)_{18}]^{2-*} \rightarrow [MAu_{24}(C{\equiv}CR)_{18-n}]^- + (C{\equiv}CR)_n^- \quad (2)$$

This special behavior of $NiAu_{24}$ is also documented in Fig. S3 and S4 (ESI†), which show typical fragmentation mass spectra for all three precursor dianions at different collision energies. In particular $NiAu_{24}$ shows strong $(C{\equiv}CR)_n^-$ signals. In terms of $RC{\equiv}C{-}C{\equiv}CR$ and $HC{\equiv}CR'$ loss, $NiAu_{24}$ behaves qualitatively the same as $PdAu_{24}$ and $PtAu_{24}$. However, the relative intensity of the minor $HC{\equiv}CR$ loss channel is higher for Ni than for Pd and Pt.

Fig. S6 (top) (ESI†) shows breakdown curves and fragment yields (on a logarithmic intensity scale) for all $[MAu_{24}(C{\equiv}CR)_{18-n}]^{2-}$ as well as $[MAu_{24}(C{\equiv}CR')(C{\equiv}CR)_{17-n}]^{2-}$ *versus* collision energy (strictly speaking the applied collision voltage). Fig. S6 (bottom) (ESI†) shows the corresponding ligand oligomer monoanion yields in the case of $NiAu_{24}$. $E_{50}$ values (50% survival yield) are 68, 77 and 84 V for the breakdown curves of $NiAu_{24}$, $PdAu_{24}$ and $PtAu_{24}$, respectively, *i.e.* M = Ni is the most labile of the three $[MAu_{24}(C{\equiv}CR)_{18}]^{2-}$ species studied. Interestingly, the $[MAu_{24}(C{\equiv}CR)_{18-n}]^{2-}$ fragment yields for $n$ = 2 and 4 (and also $n$ = 6 for Pd and Ni) show roughly the same dependence on increasing collision energy. Only after $n$ = 6 is the collision energy required for further fragmentation observed to clearly increase (roughly linearly) with $n$. Perhaps some elimination of small neutral oligomers ($n$ = 4) also occurs in the early fragmentation stages.

### 3.3 Structures of collisionally excited precursor and fragment ions

Additional cIMS measurements were carried out to further investigate the collisionally activated reactions described above, concentrating in particular on the reaction (1) cascade to form $[MAu_{24}(C{\equiv}CR)_{18-n}]^{2-}$ which is the primary dissociation process under typical experimental conditions.

**3.3.1 Coexisting isomers of vibrationally excited precursor ions, $[MAu_{24}(C{\equiv}CR)_{18}]^{2-*}$.** Fig. 3 compares arrival time distributions for all three $MAu_{24}$ precursor dianions previously subjected to different levels of collisional excitation as achieved by injecting the ions into the ion trap upstream from the cIM at variable collision voltages from 60 to 100 V. As seen in the breakdown curves discussed previously, this energy range is associated with the onset of extensive fragmentation leading to a drop of precursor dianion intensity by several orders of magnitude. Nevertheless, the dynamic range of the machine is high enough to resolve a collision energy dependent change in the ATD's of the residual, vibrationally excited $NiAu_{24}$. Whereas the measurements for M = Pd and Pt show only one, symmetric, feature throughout the injection voltage range probed, the ATD for M = Ni develops an initially weak but then clearly visible shoulder extending to longer arrival times. This feature, indicating the presence of at least one additional significantly larger structural isomer at the $m/z$ being probed,

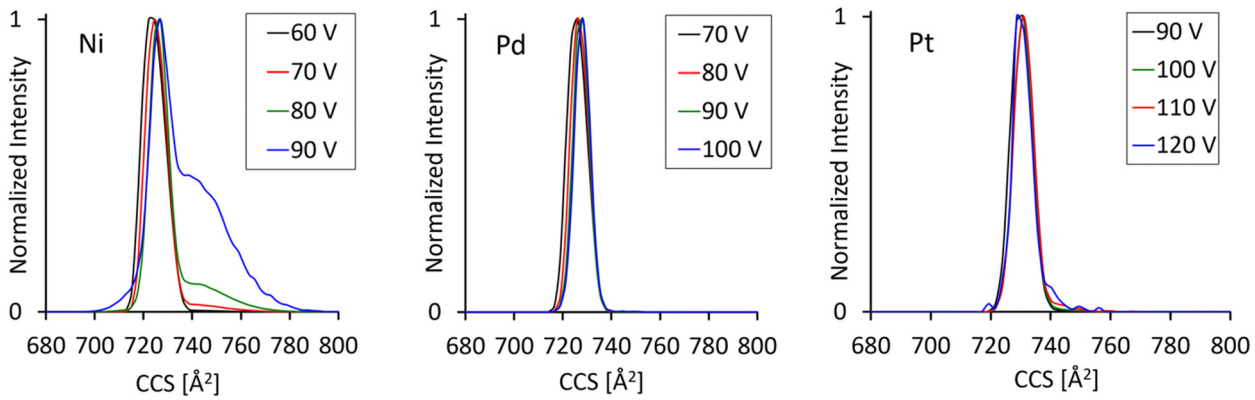


Fig. 3 Single cycle ion mobility separations for $[MAu_{24}(C{\equiv}CR)_{18}]^{2-}$ obtained for various levels of prior collisional excitation as indicated. Note the growth in relative intensity of a second resolvable isomer (or of several additional overlapping isomers) for M = Ni as internal excitation is increased and fragmentation sets in in parallel. By contrast M = Pt and Pd show no corresponding effect.

becomes dominant as the collision energy is raised further – see Fig. 3. This special behavior of $NiAu_{24}$ is likely related to its enhanced lability towards ligand oligomer anion loss as already mentioned in Section 3.2. We are exploring this further and will report in detail in a future study.[51]

It is interesting to note ref. 52 in this context. The authors of the latter study observed collision induced isomerization of $[Au_{25}(2\text{-PET})_{18}]^{\pm}$, PET = phenylethyl thiolate, to form an isomer with a *ca.* 28% larger CCS than the initial gas phase structure. This was interpreted in terms of a concerted rearrangement of the entire cluster, which has an icosahedral core/shell + staple topology analogous to that of $[MAu_{24}(C{\equiv}CR)_{18}]^{2-}$. *Ab initio* molecular dynamics (AIMD) simulations suggested that collision induced rearrangement of $[Au_{25}(2\text{-PET})_{18}]^{\pm}$ begins with a correlated rotation of the triangular faces of the icosahedral shell about the central gold atom. As the staples remain attached to the same gold atoms in this internally rotating shell, their constituent PET ligands – much like sails – are torqued and "unfurled" resulting in an isomer with a significantly larger CCS. In contrast to the case of $[Au_{25}(2\text{-PET})_{18}]^{\pm}$, we interpret our observation of isomerization at high collisional excitation of $[NiAu_{24}(C{\equiv}CR)_{18}]^{2-}$ as due to reactions which change bond connectivity in the ligands. This seems plausible as extensive loss of neutral diynes and ligand polymer anions (both involving Au-bond breaking) occurs in parallel.

### 3.3.2 $[MAu_{24}(C{\equiv}CR)_{18-n}]^{2-}$ fragments

*3.3.2.1 Single cycle separations.* We performed single cycle separations to obtain a phenomenological overview of the structural changes associated with increasing fragmentation degree, $n$ = 1–12 (for all $[MAu_{24}(C{\equiv}CR)_{18-n}]^{2-}$, resp. $[MAu_{24}(C{\equiv}CR')(C{\equiv}CR)_{17-n}]^{2-}$). The corresponding ATD's, plotted on a $^{tw}CCS_{N2}$ scale, are presented in Fig. 4.

At the comparatively low resolution accessible by a single separation cycle, the collision cross sections decrease essentially monotonically with the number of ligands lost. Note again, that odd numbered $n$ indicates the additional loss of *one* HC≡CR unit. Fig. 5 plots this trend ($^{tw}CCS_{N2}$ against $n$, the number of ligands lost) for M = Pt. The experimental data for the other two M′s show a similar monotonic CCS dropoff with $n$ (see Fig. S8, ESI†).

Remarkably (and in contrast to the isomerization of the $[NiAu_{24}(C{\equiv}CR)_{18-n}]^{2-}$ precursor dianion discussed above), $ATD_{max}$ values of specific $[MAu_{24}(C{\equiv}CR)_{18-n}]^{2-}$ fragments do not change significantly with collision energy – apart from the fact that higher collision energies are required for on average more extensive fragmentation. This suggests that an evaporative ensemble is being probed to first order.[53] Nevertheless, ATD halfwidths are already visibly $n$ and M dependent. In particular, the even numbered fragments appear on average to have significantly narrower ATD's than the odd numbered ones. Additionally, some ATD's show a reproducible (fine) structure, suggesting that the fragmentation cascade can form multiple coexisting isomers.

We attempted to model the global trend shown in Fig. 5 by sequentially removing the requisite numbers of ligands from the molecular structure (see also Fig. S9, ESI†). For this we used the converged DFT (m4 grid, PBE, def2-SVP, Disp3bj) structure of $[PdAu_{24}(C{\equiv}CR)_{18}]^{2-}$ as a starting point and generated the correspondingly defected structures by removing ligand pairs (always ligand type A and B in Scheme 1) in an otherwise

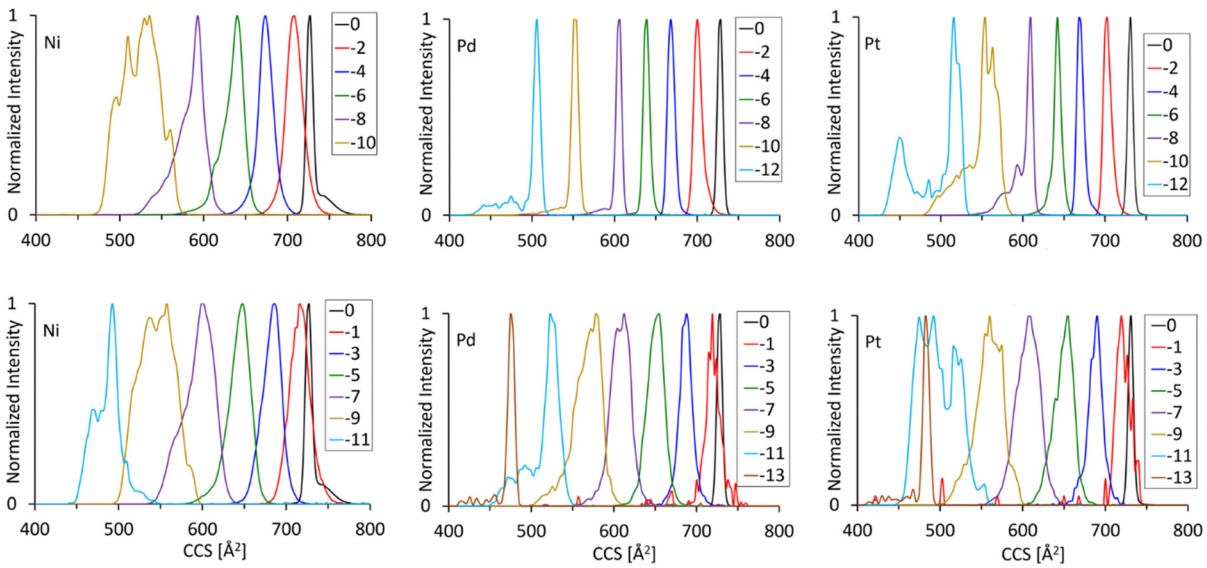


Fig. 4 Overview of single cycle arrival time distributions (ATD's) converted to a $^{tw}CCS_{N2}$ scale for $[MAu_{24}(C{\equiv}CR)_{18-n}]^{2-}$ precursor and fragment ions as a function of the number of neutral ligands lost (normalized to the most intense feature in the respective measurements). Note, that even numbered fragments correspond to one or multiple losses of neutral 1,3-diynes (RC≡C–C≡CR), R = 3,5-$(CF_3)_2C_6H_3$, *i.e.* pairs of ligands. By contrast, the odd numbered fragments correspond to (multiple) diyne loss plus loss of nominally one HC≡CR. In the case of odd numbered fragments, it is not clear at which stage in the fragmentation sequence HC≡CR is lost. Note the strong $n$- and M-dependencies of the arrival time distribution shapes even after only one separation cycle.

 

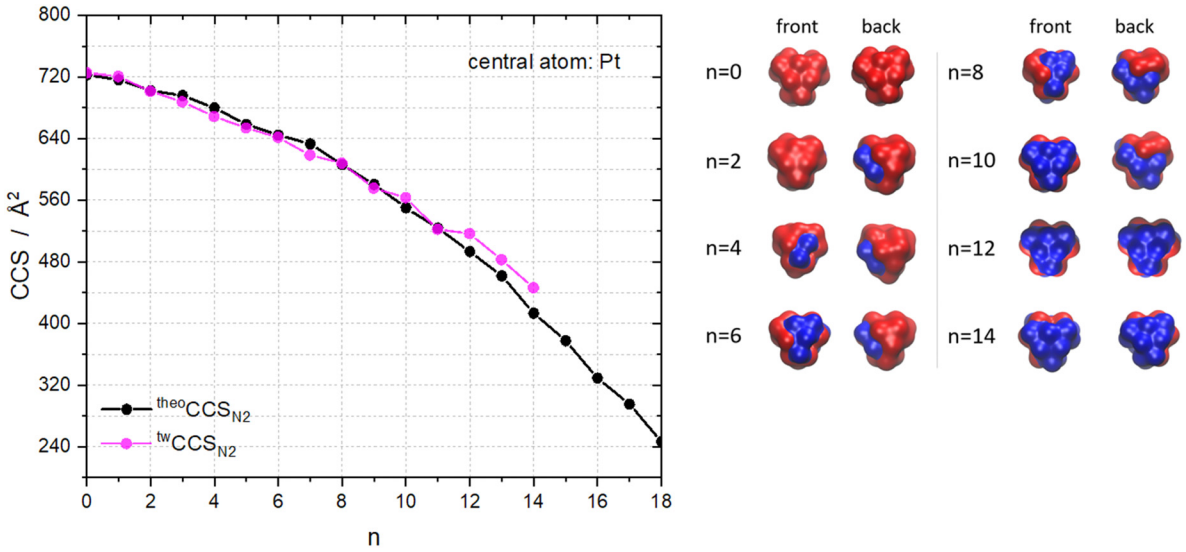


Fig. 5 Left: $^{tw}CCS_{N2}$ against $n$, the number of ligands lost to form $[PtAu_{24}(C{\equiv}CR)_{18-n}]^{2-}$ by collision induced dissociation of $[PtAu_{24}(C{\equiv}CR)_{18}]^{2-}$. Also shown are the predictions, $^{theo}CCS_{N2}$, of an atomistic model based on statistically distributed ligand loss "defects" (see text for details). Right: Schematic representations of these defected model structures for $n$ = 0 to $n$ = 14 (front and back views). The red positions refer to the terminal C-atoms of each remaining (C≡CR) ligand – neglecting the rest of the ligand in the representation. Blue positions refer to missing ligand sites (again terminal C-atom positions). Shown is the result of a "statistical" fragmentation cascade corresponding to sequential loss of pairs of adjacent ligands without further spatial correlation of the affected staples.

random sequence in the case of even $n$ and one additional arbitrarily chosen type A ligand in case of odd $n$. With these unrelaxed "defected" structures we then performed single point calculations at the GFN1 *x*TB level to generate Mulliken partial charges necessary for the trajectory method simulations of the collision cross sections. We used Pd as GFN1 *x*TB shows convergency problems with Pt in some cases. Considering that $^{theo}CCS_{N2}$ of $[PdAu_{24}(C{\equiv}CR)_{18}]^{2-}$ and $[PtAu_{24}(C{\equiv}CR)_{18}]^{2-}$ agree within the error of the trajectory calculation and no geometry optimization of the fragment is performed, this approach seems reasonable. Fig. 5 shows the resulting $^{theo}CCS_{N2}$ predictions and schematics of the defect structures for $n$ = 0–14. Apparently, the assumption of statistical ligand pair loss without further structural relaxation describes the global experimental observation – after one separation cycle – already surprisingly well.

*3.3.2.2 Multiple separation cycles.* Additional cycles of separation can be used to explore the fragment isomer space in more detail. For example, one might question whether alkyne/diyne loss is in fact always sequential, completely statistical or whether sequential eliminations are to some degree spatially correlated. Generally, the numbers, relative intensities and $^{tw}CCS_{N2}$ values of the isomers resolvable by a given number of separation cycles depend strongly on M and $n$. Selected measurements are shown in Fig. S7 (ESI†). Fig. 6 shows an extreme example for the $n$ = 10 fragment of $PtAu_{24}$, *i.e.* $[PtAu_{24}(C{\equiv}CR)_8]^{2-}$. After six separation cycles, four fragment isomers can be (partially) resolved, superposed on a broad shoulder to shorter arrival times. From smallest to largest, these isomers differ in $^{tw}CCS_{N2}$ by *ca.* 3%. They are formed roughly in the intensity ratio 5 : 3 : 2 : 1.

To put this observation into perspective it is important to remember that there are initially six $Au_2(C{\equiv}CR)_3$ "staples" (each with an $Au_2$ unit and three C≡CR ligands). After loss of 10 ligands and assuming no structural relaxation occurs, multiple $[PtAu_{24}(C{\equiv}CR)_8]^{2-}$ isomer types can result which are distinguishable by the partitioning of their 8 remaining ligands over the cluster "surface" (in principle $Au_2$ units can host 3, 2, 1 or 0 remaining ligands subject to the restriction that there are only 8 ligands left overall). Table S2 (ESI†) lists examples of the seven possible isomer types ordered according to number of ligands left on each of the six staples. Obviously, there are a large number of different combinatorial possibilities for each isomer type depending on whether ligand loss is completely random or somehow spatially correlated (the $Au_2(C{\equiv}CR)_3$ staples themselves are initially indistinguishable due to molecular symmetry). Many of these combinatorial possibilities will have distinguishable patches of ligand-free surface regions and corresponding CCS values. It goes beyond the scope of this study to consider all combinatorial possibilities but it is nevertheless of interest to compare the experimentally resolved CCS spread to the predictions for several different isomers resulting from various assumed fragmentation sequences – ranging from fully correlated in space (*i.e.* a sequence of A + B or B + C ligand losses (see Scheme 1) to form diynes progressing from staple to adjacent staple) to purely statistical (10 of 18 monomers are randomly removed regardless of which staple/position they originate from).

For this, we calculated $^{theo}CCS_{N2}$ for nine possible $[PtAu_{24}(C{\equiv}CR)_8]^{2-}$ isomers generated by removing either

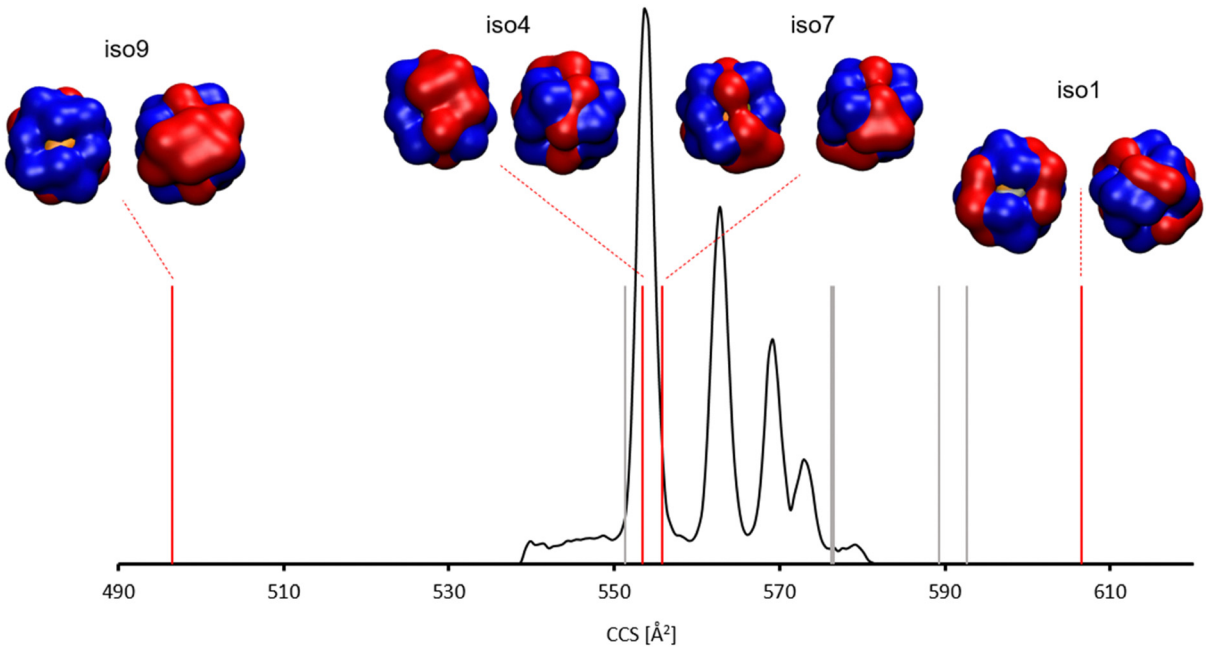


Fig. 6 Example of resolved isomers formed upon CID of $[PtAu_{24}(C{\equiv}CR)_{18}]^{2-}$ for the $n$ = 10 fragment, *i.e.* $[PtAu_{24}(C{\equiv}CR)_{8}]^{2-}$ after six cIM separation cycles. The vertical lines refer to $^{theo}CCS_{N2}$ values calculated for possible isomers as listed in Table S2 (ESI†). The red bars highlight largest, smallest and two intermediate sized structural models for which we show the structure. The corresponding defect structures are shown from the front and back side (see the caption of Fig. 5 for details on the schematic representation). Other defect model structures are shown in Fig. S10 (ESI†).

three, two, one or zero C≡CR ligands from the staples – otherwise with the same method as already described above. Fig. 6 presents the $^{theo}CCS_{N2}$ values of the nine calculated isomers (see also Table S2 and Fig. S10 which shows schematics of the corresponding structures, ESI†). The smallest $^{theo}CCS_{N2}$ is found for isomer 9 (496.5 Å$^2$) in which the ligands have been removed from one side of the cluster only in a non-statistical pattern. The largest isomer (isomer 1, 606.6 Å$^2$) is obtained when 2 of the staples stay complete, one ligand is removed from a third staple and all ligands are removed from the remaining three staples. Doing the same, but with a spatially more correlated loss sequence, results in a $^{theo}CCS_{N2}$ of 551.3 Å$^2$, *i.e.* 9% smaller (isomer 8). Interestingly, the experimental $[PdAu_{24}(C{\equiv}CR)_{8}]^{2-}$ isomer spread lies well between the limits of isomer 1 and isomer 9. Overall, it seems that the best agreement with the experiment is obtained when radical formation is minimized. In particular isomer 4 (five adjacent pairs of ligands are lost; 553.4 Å$^2$) and isomer 7 (4 adjacent pairs and 2 singles are lost; 555.8 Å$^2$) have $^{theo}CCS_{N2}$ which are very close to the most intense isomer found in the experiment.

To summarize: we can rule out extensive fragmentation to form highly anisotropic $[PtAu_{24}(C{\equiv}CR)_{8}]^{2-}$ structures. Furthermore, the observed isomer spread is inconsistent with random monomer loss and instead points to mainly diyne evolution by way of loss of pairs of adjacent ligands on a given staple. However, it remains unclear whether in the fragmentation sequence the next diyne loss is spatially correlated to the previous one. Further insight, also into relative isomer intensities and into the behavior at intermediate fragment sizes, requires much more extensive modelling which will be the subject of a future study.

## Summary and conclusions

Collision induced dissociation, high resolution cyclic ion mobility mass spectrometry and trajectory simulations based on quantum chemical calculations were used to compare the structures of isolated $[MAu_{24}(C{\equiv}CR)_{18}]^{2-}$ (M = Ni, Pd and Pt) and of the associated fragment ions. The resolution of cIMS is high enough to allow differentiation of the three different transition metal doped precursor dianions on the basis of purely their collision cross sections. The size trend observed for the gas phase dianions is consistent with X-ray crystallography which shows that in the ionic solid (held together by $PPh_4^+$ countercations), the $[MAu_{24}(C{\equiv}CR)_{18}]^{2-}$ molecules have a common geometry but slightly M-dependent M–Au bond distances.

All three $[MAu_{24}(C{\equiv}CR)_{18}]^{2-}$ dianions fragment to $[MAu_{24}(C{\equiv}CR)_{18-n}]^{2-}$ species – with even numbered $n$ losses strongly favored. This and the dependence of fragmentation degree on collision energy argues for primarily sequential diyne loss. Up to 12 ligands, *i.e.* formally 6 RC≡C–C≡CR diyne moieties can be eliminated in this fashion. Cyclic IMS measurements show that the resulting $[MAu_{24}(C{\equiv}CR)_{18-n}]^{2-}$ isomer distributions are strongly $n$- and M-dependent. Preliminary analysis is consistent with an underlying process involving elimination from staples of pairs of neighbouring ligands.

Future MD simulations will be required to help establish whether sequential ligand/diyne eliminations continue in a spatially correlated fashion.

$[NiAu_{24}(C{\equiv}CR)_{18}]^{2-}$ also fragments significantly by loss of ligand oligomers, $(C{\equiv}CR)_n^-$ with $n$ ranging up to 10. In parallel, it can undergo measurable isomerization to generate isobaric species with significantly larger collision cross sections (a process not observed for M = Pd and Pt). We will report further details in a future publication.

## Conflicts of interest

There are no conflicts to declare.

## Acknowledgements

MK acknowledges support of this work by DFG under CRC 1441 ''TrackAct'', project A2 and CRC 1573 ''4f-for-future'' projects C1 and C3. Additionally, MK and PW are grateful to KIT, Land B.-W. and DFG for the funding of a Waters Cyclic IMS system under Art. 91b GG without which this study would not have been possible. TT thanks JST, CREST (Grant No. JPMJCR20B2) for financial support of this work. SI acknowledges the financial support by JSPS KAKENHI (JP21J20631).

## References

1 J. J. Zhao, Q. Y. Du, S. Zhou and V. Kumar, Endohedrally Doped Cage Clusters, *Chem. Rev.*, 2020, **120**(17), 9021–9163.
2 T. Weiske, D. K. Böhme, J. Hrusak, W. Krätschmer and H. Schwarz, Endohedral Cluster Compounds – Inclusion of Helium within C60+ and C70+ through Collision Experiments, *Angew. Chem., Int. Ed. Engl.*, 1991, **30**(7), 884–886.
3 H. Shinohara, Endohedral metallofullerenes, *Rep. Prog. Phys.*, 2000, **63**(6), 843–892.
4 S. Furuse, K. Koyasu, J. Atobe and A. Nakajima, Experimental and theoretical characterization of $MSi_{16}^-$, $MGe_{16}^-$, $MSn_{16}^-$, and $MPb_{16}^-$ (M = Ti, Zr, and Hf): The role of cage aromaticity, *J. Chem. Phys.*, 2008, **129**(6), 6.
5 L. M. Wang, J. Bai, A. Lechtken, W. Huang, D. Schooss, M. M. Kappes, X. C. Zeng and L. S. Wang, Magnetic doping of the golden cage cluster $M@Au_{16}^-$ (M = Fe,Co,Ni), *Phys. Rev. B*, 2009, **79**(3), 4.
6 C. A. Fields-Zinna, M. C. Crowe, A. Dass, J. E. F. Weaver and R. W. Murray, Mass Spectrometry of Small Bimetal Monolayer-Protected Clusters, *Langmuir*, 2009, **25**(13), 7704–7710.
7 B. K. Teo, H. Zhang and X. B. Shi, Design, Synthesis, and Structure of the Largest Trimetallic Cluster, $[(PH_3P)_{10}Au_{12}Ag_{12}PtCl_7]Cl$ – The First Example of a Trimetallic Biicosahedral Supracluster and Its Implication for the Vertex-Sharing Polyicosahedral Growth of the Au/Ag/Pt Ternary Cluster System, *J. Am. Chem. Soc.*, 1993, **115**(18), 8489–8490.
8 J. J. Bour, R. P. F. Kanters, P. P. J. Schlebos and J. J. Steggerda, Mixed platinum-gold clusters – Synthesis, structure and properties of $PtAu_8(PPh_3)_8(NO_3)_2$, *Recl. Trav. Chim. Pays-Bas-J. Roy. Neth. Chem. Soc*, 1988, **107**(3), 211–215.
9 T. Kawawaki, Y. Imai, D. Suzuki, S. Kato, I. Kobayashi, T. Suzuki, R. Kaneko, S. Hossain and Y. Negishi, Atomically Precise Alloy Nanoclusters, *Chem. – Eur. J.*, 2020, **26**(69), 16150–16193.
10 S. Ito, K. Koyasu, S. Takano and T. Tsukuda, Collision-Induced Reductive Elimination of 1,3-Diynes from $[MAu_{24}(C{\equiv}CR)_{18}]^{2-}$ (M = Pd, Pt) Yielding Clusters of Superatoms, *J. Phys. Chem. C*, 2020, **124**(35), 19119–19125.
11 S. Takano, S. Ito and T. Tsukuda, Efficient and Selective Conversion of Phosphine-Protected $(MAu_8)^{2+}$ (M = Pd, Pt) Superatoms to Thiolate-Protected $(MAu_{12})^{6+}$ or Alkynyl-Protected $(MAu_{12})^{4+}$ Superatoms via Hydride Doping, *J. Am. Chem. Soc.*, 2019, **141**(40), 15994–16002.
12 S. Takano, E. Ito, T. Nakamura and T. Tsukuda, Effect of Group-10 Element M (Ni, Pd, Pt) on Electronic Structure of Icosahedral $M@Au_{12}$ Cores of $MAu_{24}L_{18}$ (L = Alkynyl, Thiolate), *J. Phys. Chem. C*, 2023, 7.
13 Y. Negishi, W. Kurashige, Y. Niihori, T. Iwasa and K. Nobusada, Isolation, structure, and stability of a dodecanethiolate-protected $Pd_1Au_{24}$ cluster, *Phys. Chem. Chem. Phys.*, 2010, **12**(23), 6219–6225.
14 M. A. Tofanelli, T. W. Ni, B. D. Phillips and C. J. Ackerson, Crystal Structure of the $PdAu_{24}(SR)_{18}^0$ Superatom, *Inorg. Chem.*, 2016, **55**(3), 999–1001.
15 H. F. Qian, D. E. Jiang, G. Li, C. Gayathri, A. Das, R. R. Gil and R. C. Jin, Monoplatinum Doping of Gold Nanoclusters and Catalytic Application, *J. Am. Chem. Soc.*, 2012, **134**(39), 16159–16162.
16 S. B. Tian, L. W. Liao, J. Y. Yuan, C. H. Yao, J. S. Chen, J. L. Yang and Z. K. Wu, Structures and magnetism of mono-palladium and mono-platinum doped $Au_{25}(PET)_{18}$ nanoclusters, *Chem. Commun.*, 2016, **52**(64), 9873–9876.
17 K. Kwak, Q. Tang, M. Kim, D. E. Jiang and D. Lee, Interconversion between Superatomic 6-Electron and 8-Electron Configurations of $M@Au_{24}(SR)_{18}$ Clusters (M = Pd, Pt), *J. Am. Chem. Soc.*, 2015, **137**(33), 10833–10840.
18 M. M. Kappes, R. W. Kunz and E. Schumacher, Production of large Sodium Clusters ($Na_x$, $x \leq 65$) by Seeded Beam Expansions, *Chem. Phys. Lett.*, 1982, **91**(6), 413–418.
19 W. D. Knight, K. Clemenger, W. A. de Heer, W. A. Saunders, M. Y. Chou and M. L. Cohen, Electronic Shell Structure and Abundances of Sodium Clusters, *Phys. Rev. Lett.*, 1984, **52**(24), 2141–2143.
20 M. Walter, J. Akola, O. Lopez-Acevedo, P. D. Jadzinsky, G. Calero, C. J. Ackerson, R. L. Whetten, H. Gronbeck and H. Häkkinen, A unified view of ligand-protected gold clusters as superatom complexes, *Proc. Natl. Acad. Sci. U. S. A.*, 2008, **105**(27), 9157–9162.
21 S. B. Zhang, M. L. Cohen and M. Y. Chou, Electronic shell structure of simple metal heteroclusters, *Phys. Rev. B: Condens. Matter Mater. Phys.*, 1987, **36**(6), 3455–3458.
22 M. M. Kappes, P. Radi, M. Schar and E. Schumacher, Probes for electronic and geometrical shell structure effects in

alkali-metal clusters – photoionization measurements on $K_xLi$, $K_xMg$ and $K_xZn$ ($x \leq 25$), *Chem. Phys. Lett.*, 1985, **119**(1), 11–16.
23 C. Baladron and J. A. Alonso, Stability and Magic Numbers of Hetero-Atomic Clusters of Simple Metals, *Physica B*, 1988, **154**(1), 73–81.
24 E. Janssens, S. Neukermans and P. Lievens, Shells of electrons in metal doped simple metal clusters, *Curr. Opin. Solid State Mat. Sci.*, 2004, **8**(3–4), 185–193.
25 B. C. Bohrer, S. I. Mererbloom, S. L. Koeniger, A. E. Hilderbrand and D. E. Clemmer, Biomolecule Analysis by Ion Mobility Spectrometry, *Annu. Rev. Anal. Chem.*, 2008, **1**, 293–327.
26 B. J. Gregory and C. K. Ingold, Mechanism of Electrophilic Substitution at a Saturated Carbon Atom. Part XI. Bimolecular and Unimolecular Substitution of Mercury for Gold in Alkylgold Complexes, *J. Chem. Soc. B*, 1969, 276.
27 M. C. Brandys, M. C. Jennings and R. J. Puddephatt, Luminescent gold(I) macrocycles with diphosphine and 4,4′-bipyridyl ligands, *J. Chem. Soc., Dalton Trans.*, 2000, **24**, 4601–4606.
28 S. Takano, H. Hirai, S. Muramatsu and T. Tsukuda, Hydride-Mediated Controlled Growth of a Bimetallic $(Pd@Au_8)^{2+}$ Superatom to a Hydride-Doped $(HPd@Au_{10})^{3+}$ Superatom, *J. Am. Chem. Soc.*, 2018, **140**(39), 12314–12317.
29 K. Giles, J. Ujma, J. Wildgoose, S. Pringle, K. Richardson, D. Langridge and M. Green, A Cyclic Ion Mobility-Mass Spectrometry System, *Anal. Chem.*, 2019, **91**(13), 8564–8573.
30 E. A. M. Mason and E. W. McDaniel, *Transport Properties of Ions in Gases*, Wiley, New York, Chichester, Brisbane, Toronto, Singapore, 1988.
31 P. Weis, L. Fercic and M. Kappes, to be published.
32 C. Larriba and C. J. Hogan, Free molecular collision cross section calculation methods for nanoparticles and complex ions with energy accommodation, *J. Comput. Phys.*, 2013, **251**, 344–363.
33 C. Larriba-Andaluz and C. J. Hogan, Collision cross section calculations for polyatomic ions considering rotating diatomic/linear gas molecules, *J. Chem. Phys.*, 2014, **141**(19), 9.
34 R. Ahlrichs, M. Bär, M. Häser, H. Horn and C. Kölmel, Electronic-Structure calculations on Workstation Computers – The Program System Turbomole, *Chem. Phys. Lett.*, 1989, **162**(3), 165–169.
35 P. A. M. Dirac, The quantum theory of the electron, *Proc. R. Soc. London, Ser. A*, 1928, **117**(778), 610–624.
36 J. C. Slater, A simplification of the Hartree-Fock method, *Phys. Rev.*, 1951, **81**(3), 385.
37 J. P. Perdew, K. Burke and M. Ernzerhof, Generalized gradient approximation made simple (vol 77, pg 3865, 1996), *Phys. Rev. Lett.*, 1997, **78**(7), 1396.
38 J. P. Perdew and Y. Wang, Accurate and simple analytic representation of the electron-gas correlation energy, *Phys. Rev. B: Condens. Matter Mater. Phys.*, 1992, **45**(23), 13244.
39 A. Hellweg and D. Rappoport, Development of new auxiliary basis functions of the Karlsruhe segmented contracted basis sets including diffuse basis functions (def2-SVPD, def2-TZVPPD, and def2-QVPPD) for RI-MP2 and RI-CC calculations, *Phys. Chem. Chem. Phys.*, 2015, **17**(2), 1010–1017.
40 S. Grimme, J. Antony, S. Ehrlich and H. Krieg, A consistent and accurate ab initio parametrization of density functional dispersion correction (DFT-D) for the 94 elements H–Pu, *J. Chem. Phys.*, 2010, **132**(15), 19.
41 S. Grimme, S. Ehrlich and L. Goerigk, Effect of the Damping Function in Dispersion Corrected Density Functional Theory, *J. Comput. Chem.*, 2011, **32**(7), 1456–1465.
42 C. Bannwarth, E. Caldeweyher, S. Ehlert, A. Hansen, P. Pracht, J. Seibert, S. Spicher and S. Grimme, Extended tight-binding quantum chemistry methods, *Wiley Interdiscip. Rev.-Comput. Mol. Sci.*, 2021, **11**(2), 49.
43 S. Grimme, C. Bannwarth and P. Shushkov, A Robust and Accurate Tight-Binding Quantum Chemical Method for Structures, Vibrational Frequencies, and Noncovalent Interactions of Large Molecular Systems Parametrized for All spd-Block Elements ($Z$ = 1–86), *J. Chem. Theory Comput.*, 2017, **13**(5), 1989–2009.
44 S. Ito, K. Koyasu, S. Takano and T. Tsukuda, Critical Role of $CF_3$ Groups in the Electronic Stabilization of $[PdAu_{24}(C \equiv C_6H_3(CF_3)_2)_{18}]^{2-}$ as Revealed by Gas-Phase Anion Photoelectron Spectroscopy, *J. Phys. Chem. Lett.*, 2021, **12**(42), 10417–10421.
45 Jmol: an open-source Java viewer for chemical structures in 3D, **https://www.jmol.org/**.
46 Calculate Root-mean-square deviation (RMSD) of Two Molecules Using Rotation, Github, **https://github.com/charnley/rmsd**, 1.5.1.
47 W. Humphrey, A. Dalke and K. Schulten, VMD: Visual molecular dynamics, *J. Mol. Graphics*, 1996, **14**(1), 33–38.
48 Z. D. Xu, T. Nakane and H. Shinohara, Production and isolation of Ca@C-82 (I-IV) and Ca@C-84 (I,II) metallofullerenes, *J. Am. Chem. Soc.*, 1996, **118**(45), 11309–11310.
49 A. Baksi, E. K. Schneider, P. Weis, I. Chakraborty, O. Fuhr, S. Lebedkin, W. J. Parak and M. M. Kappes, Linear Size Contraction of Ligand Protected Ag-29 Clusters by Substituting Ag with Cu, *ACS Nano*, 2020, **14**(11), 15064–15070.
50 Y. Zeng, S. Havenridge, M. Gharib, A. Baksi, K. Weerawardene, A. R. Ziefuss, C. Strelow, C. Rehbock, A. Mews, S. Barcikowski, M. M. Kappes, W. J. Parak, C. M. Aikens and I. Chakraborty, Impact of Ligands on Structural and Optical Properties of $Ag_{29}$ Nanoclusters, *J. Am. Chem. Soc.*, 2021, **143**(25), 9405–9414.
51 F. Hennrich, S. Ito, P. Weis, M. Neumaier, S. Takano, T. Tsukuda and M. M. Kappes, to be published.
52 E. Kalenius, S. Malola, M. F. Matus, R. Kazan, T. Bürgi and H. Häkkinen, Experimental Confirmation of a Topological Isomer of the Ubiquitous $Au_{25}(SR)_{18}$ Cluster in the Gas Phase, *J. Am. Chem. Soc.*, 2021, **143**(3), 1273–1277.
53 C. E. Klots, Temperatures of Evaporating Clusters, *Nature*, 1987, **327**(6119), 222–223.

 